



Implementing the Quantum von Neumann Architecture with Superconducting Circuits

Matteo Mariani *et al.*

Science **334**, 61 (2011);

DOI: 10.1126/science.1208517

This copy is for your personal, non-commercial use only.

If you wish to distribute this article to others, you can order high-quality copies for your colleagues, clients, or customers by [clicking here](#).

Permission to republish or repurpose articles or portions of articles can be obtained by following the guidelines [here](#).

The following resources related to this article are available online at www.sciencemag.org (this information is current as of January 23, 2013):

Updated information and services, including high-resolution figures, can be found in the online version of this article at:

<http://www.sciencemag.org/content/334/6052/61.full.html>

Supporting Online Material can be found at:

<http://www.sciencemag.org/content/suppl/2011/08/31/science.1208517.DC1.html>

A list of selected additional articles on the Science Web sites **related to this article** can be found at:

<http://www.sciencemag.org/content/334/6052/61.full.html#related>

This article **cites 24 articles**, 2 of which can be accessed free:

<http://www.sciencemag.org/content/334/6052/61.full.html#ref-list-1>

This article has been **cited by** 2 articles hosted by HighWire Press; see:

<http://www.sciencemag.org/content/334/6052/61.full.html#related-urls>

This article appears in the following **subject collections**:

Physics

<http://www.sciencemag.org/cgi/collection/physics>

16. N. Wiebe, D. W. Berry, P. Hoyer, B. C. Sanders, <http://arxiv.org/abs/1011.3489> (2010).
17. M. Nielsen, I. Chuang, *Quantum Computation and Quantum Information* (Cambridge Univ. Press, Cambridge, 2001).
18. A. Steane, *Nature* **399**, 124 (1999).
19. A. Auerbach, *Interacting Electrons and Quantum Magnetism* (Springer, New York, 1994).
20. P. Schindler *et al.*, *Science* **332**, 1059 (2011).
21. H. F. Trotter, *Proc. Am. Math. Soc.* **10**, 545 (1959).
22. S. Lloyd, L. Viola, *Phys. Rev. A* **65**, 010101 (2001).
23. Materials and methods are available as supporting material on Science Online.
24. A. Sørensen, K. Mølmer, *Phys. Rev. Lett.* **82**, 1971 (1999).
25. J. Benhelm, G. Kirchmair, C. F. Roos, R. Blatt, *Nat. Phys.* **4**, 463 (2008).
26. D. Porras, J. I. Cirac, *Phys. Rev. Lett.* **92**, 207901 (2004).
27. J. F. Poyatos, J. I. Cirac, P. Zoller, *Phys. Rev. Lett.* **78**, 390 (1997).
28. A. G. White *et al.*, *J. Opt. Soc. Am. B* **24**, 172 (2007).
29. W. Dür, G. Vidal, J. I. Cirac, *Phys. Rev. A* **62**, 062314 (2000).
30. I. Kassal, J. D. Whitfield, A. Perdomo-Ortiz, M.-H. Yung, A. Aspuru-Guzik, *Annu. Rev. Phys. Chem.* **62**, 185 (2011).
31. C. Nayak, S. H. Simon, A. Stern, M. Freedman, S. Das Sarma, *Rev. Mod. Phys.* **80**, 1083 (2008).
32. H. F. Hofmann, *Phys. Rev. Lett.* **94**, 160504 (2005).
33. T. Monz *et al.*, *Phys. Rev. Lett.* **102**, 040501 (2009).
34. A. Gilchrist, N. K. Langford, M. A. Nielsen, *Phys. Rev. A* **71**, 062310 (2005).
35. J. P. Home *et al.*, *Science* **325**, 1227 (2009).

Acknowledgments: We thank W. Dür, A. Aspuru-Guzik, and M. Brownnutt for discussions. We acknowledge financial

support by the Austrian Science Fund (FWF) [SFB F40 FOQUS], the Institut für Quanteninformation GmbH, Intelligence Advanced Research Projects Activity, and the European Commission for support via the integrated project AQUTE, two Marie Curie International Incoming Fellowships, and the ERC advanced grant CRYTERION.

Supporting Online Material

www.sciencemag.org/cgi/content/full/science.1208001/DC1
SOM Text
Figs. S1 to S9
Tables S1 to S6
References

6 May 2011; accepted 14 July 2011

Published online 1 September 2011;

10.1126/science.1208001

Implementing the Quantum von Neumann Architecture with Superconducting Circuits

Matteo Mariani^{1,4*}, H. Wang,^{1†} T. Yamamoto,^{1,2} M. Neeley,^{1‡} Radosław C. Bialczak,¹ Y. Chen,¹ M. Lenander,¹ Erik Lucero,¹ A. D. O'Connell,¹ D. Sank,¹ M. Weides,^{1§} J. Wenner,¹ Y. Yin,¹ J. Zhao,¹ A. N. Korotkov,³ A. N. Cleland,^{1,4} John M. Martinis^{1,4*}

The von Neumann architecture for a classical computer comprises a central processing unit and a memory holding instructions and data. We demonstrate a quantum central processing unit that exchanges data with a quantum random-access memory integrated on a chip, with instructions stored on a classical computer. We test our quantum machine by executing codes that involve seven quantum elements: Two superconducting qubits coupled through a quantum bus, two quantum memories, and two zeroing registers. Two vital algorithms for quantum computing are demonstrated, the quantum Fourier transform, with 66% process fidelity, and the three-qubit Toffoli-class OR phase gate, with 98% phase fidelity. Our results, in combination especially with longer qubit coherence, illustrate a potentially viable approach to factoring numbers and implementing simple quantum error correction codes.

Quantum processors (1–4) based on nuclear magnetic resonance (5–7), trapped ions (8–10), and semiconducting devices (11) were used to realize Shor's quantum factoring algorithm (5) and quantum error correction (6, 8). The quantum operations underlying these algorithms include two-qubit gates (2, 3), the quantum Fourier transform (7, 9), and three-qubit Toffoli gates (10, 12). In addition to a quantum processor, a second critical element for a quantum machine is a quantum memory, which has

been demonstrated, for example, using optical systems to map photonic entanglement into and out of atomic ensembles (13).

Superconducting quantum circuits (14) have met a number of milestones, including demonstrations of two-qubit gates (15–20) and the advanced control of both qubit and photonic quantum states (19–22). We demonstrate a superconducting integrated circuit that combines a processor—executing the quantum Fourier transform and a three-qubit Toffoli-class OR phase gate—with a memory and a zeroing register in a single device. This combination of a quantum central processing unit (quCPU) and a quantum random-access memory (quRAM), which comprise two key elements of a classical von Neumann architecture, defines our quantum von Neumann architecture.

In our architecture (Fig. 1A), the quCPU performs one-, two-, and three-qubit gates that process quantum information, and the adjacent quRAM allows quantum information to be written, read out, and zeroed. The quCPU includes two superconducting phase qubits (18, 19, 21, 22), Q_1 and Q_2 , connected through a coupling bus provided by a superconducting microwave resonator B. The quRAM comprises two superconducting resona-

tors M_1 and M_2 that serve as quantum memories, as well as a pair of zeroing registers Z_1 and Z_2 , two-level systems that are used to dump quantum information. The chip geometry is similar to that in (21, 22), with the addition of the two zeroing registers. Figure 1B shows the characterization of the device by means of swap spectroscopy (21).

The computational capability of our architecture is displayed in Fig. 2A, where a seven-channel quantum circuit, yielding a 128-dimensional Hilbert space, executes a prototypical algorithm. First, we create a Bell state between Q_1 and Q_2 using a series of π -pulse, \sqrt{i} SWAP (entangling state), and i SWAP (exchanging state) operations (step I, a to c) (22). The corresponding density matrix $\hat{\rho}_{(I)}$ [Fig. 2C (I)] is measured by quantum state tomography. The Bell state is then written into the quantum memories M_1 and M_2 by an i SWAP pulse (step II) (22), leaving the qubits in their ground states $|g\rangle$, with density matrix $\hat{\rho}_{(II)}$ [Fig. 2C (II)]. While storing the first Bell state in M_1 and M_2 , a second Bell state with density matrix $\hat{\rho}_{(III)}$ [Fig. 2C (III)] is created between the qubits, using a sequence similar to the first operation (step III, a to c).

To reuse the qubits Q_1 and Q_2 , for example to read out the quantum information stored in the memories M_1 and M_2 , the second Bell state has to be dumped (23). This is accomplished using two zeroing gates, by bringing Q_1 on resonance with Z_1 and Q_2 with Z_2 for a zeroing time τ_z , corresponding to a full i SWAP (step IV). Figure 2B shows the corresponding dynamics, where each qubit, initially in the excited state $|e\rangle$, is measured in the ground state $|g\rangle$ after ≈ 30 ns. The density matrix $\hat{\rho}_{(IV)}$ of the zeroed two-qubit system is shown in Fig. 2C (IV). Once zeroed, the qubits can be used to read the memories (step V), allowing us to verify that, at the end of the algorithm, the stored state is still entangled. This is clearly demonstrated by the density matrix shown in Fig. 2C (V).

The ability to store entanglement in the memories, which are characterized by much longer coherence times than the qubits, is key to the quantum von Neumann architecture. We demonstrate this capability in Fig. 2, D and E, where the fidelity and concurrence metrics (24) of the Bell states stored in M_1 and M_2 are compared with

¹Department of Physics, University of California, Santa Barbara, CA 93106–9530, USA. ²Green Innovation Research Laboratories, NEC Corporation, Tsukuba, Ibaraki 305-8501, Japan. ³Department of Electrical Engineering, University of California, Riverside, CA 92521, USA. ⁴California NanoSystems Institute, University of California, Santa Barbara, CA 93106–9530, USA.

*To whom correspondence should be addressed. E-mail: matmar@physics.ucsb.edu (M.M.); martinis@physics.ucsb.edu (J.M.M.)

†Present address: Department of Physics, Zhejiang University, Hangzhou 310027, China.

‡Present address: Lincoln Laboratory, Massachusetts Institute of Technology, 244 Wood Street, Lexington, MA 02420–9108, USA.

§Present address: National Institute of Standards and Technology, Boulder, CO 80305, USA.

those for the same states stored in Q_1 and Q_2 . The experiment is performed as in Fig. 2A, but eliminating steps (III) and (IV) for memory storage, and steps (II) to (V) for qubit storage. For the qubits, the storage time τ_{st} is defined as the wait time at the end of step (I), before measuring the qubit states, whereas for the resonators the wait time is that between the write and read steps. The fidelity of the qubit states decays to below 0.2 after 400 ns, whereas for the states stored in the memories it remains above 0.4 up to ≈ 1.5 μs . Most important, after only 100 ns the state stored in the qubits does not preserve any entanglement, as indicated by a zero concurrence, whereas the memories retain their entanglement for at least 1.5 μs (Fig. 2E). We expect to take advantage of our architecture in long computations, where qubit states can be protected and reused by writing them into, and reading them out of, the long-lived quRAM.

Two-qubit gates are a vital resource for the operation of the quCPU (2, 3). A variety of such gates have been implemented in superconducting circuits (15–20), with some recent demonstrations of quantum algorithms (16, 18). Control Z - π (CZ - π) gates are readily realizable with superconducting qubits, due to easy access to the third energy state of the qubit, effectively operating the qubit as a qutrit (16, 18, 20, 25). However, CZ - π gates are just a subset of the more general

class of CZ - ϕ gates, obtained for the special case where the phase $\phi = \pi$. In our architecture, the full class of CZ - ϕ gates, with ϕ from ≈ 0 to π , can be generated by coupling a qutrit close to resonance with a bus resonator.

Figure 3A shows the quantum logic circuit that generates the CZ - ϕ gate (left) and a shorthand symbol for the gate (right). The logic circuit demonstrates the nontrivial case where qubits Q_1 and Q_2 are brought from their initial ground state to $|Q_1Q_2\rangle = |ee\rangle$ by applying a π -pulse to each qubit. The excitation in Q_2 is then transferred into bus resonator B, and Q_1 's $|e\rangle \leftrightarrow |f\rangle$ transition is brought close to resonance with B for the time required for a 2π rotation, where the states $|Q_1B\rangle = |e1\rangle$ and $|f0\rangle$ are detuned by a frequency δ_{Q_1B} , which we term a “semiresonant condition.” In this process, Q_1 acquires the phase (26)

$$\phi = \pi - \pi \frac{\delta_{Q_1B}}{\sqrt{\delta_{Q_1B}^2 + \tilde{g}_{Q_1B}^2}} \quad (1)$$

where \tilde{g}_{Q_1B} is the coupling frequency between $|e1\rangle$ and $|f0\rangle$. The final step is to move the excitation from B back into Q_2 .

The time-domain swaps of $|Q_1B\rangle$ between the states $|e1\rangle$ and $|f0\rangle$ are shown in Fig. 3B, where the solid black line indicates the detunings and corresponding interaction times used to gener-

ate any phase $0 \leq \phi \leq \pi$ (ideally $\phi \rightarrow 0$ when $\delta_{Q_1B} \rightarrow \infty$). These phases are measured by performing two Ramsey experiments on Q_1 for each value of the detuning δ_{Q_1B} , one with B in the $|0\rangle$ state, and the other with B in the $|1\rangle$ state. The relative phase between the Ramsey fringes corresponds to the value of ϕ for the CZ - ϕ gate (26), as shown in Fig. 3C.

A more sophisticated version of this experiment is performed by initializing Q_1 and Q_2 each in the superposition state $|g\rangle + |e\rangle$. We move Q_2 's state into B, perform a CZ - ϕ gate with $0 \leq \phi \leq \pi$, move the state in B back into Q_2 , rotate Q_1 's resulting state by $\pi/2$ about the y axis, and perform a joint measurement of Q_1 and Q_2 . Ideally, this protocol permits the creation of two-qubit states ranging from a product state for $\phi = 0$ to a maximally entangled state for $\phi = \pi$. In the two-qubit basis set $M_2 = \{|gg\rangle, |eg\rangle, |ge\rangle, |ee\rangle\}$, the general density matrix of such two-qubit states reads

$$\hat{\rho}_\phi = \begin{pmatrix} 0 & 0 & 0 & 0 \\ 0 & 1/2 & (1 - e^{-i\phi})/4 & (1 + e^{-i\phi})/4 \\ 0 & (1 - e^{i\phi})/4 & (1 - \cos\phi)/4 & (-i \sin\phi)/4 \\ 0 & (1 + e^{i\phi})/4 & (i \sin\phi)/4 & (1 + \cos\phi)/4 \end{pmatrix} \quad (2)$$

Figure 3D shows the fidelity and entanglement of formation (EOF) (24) of two-qubit states generated

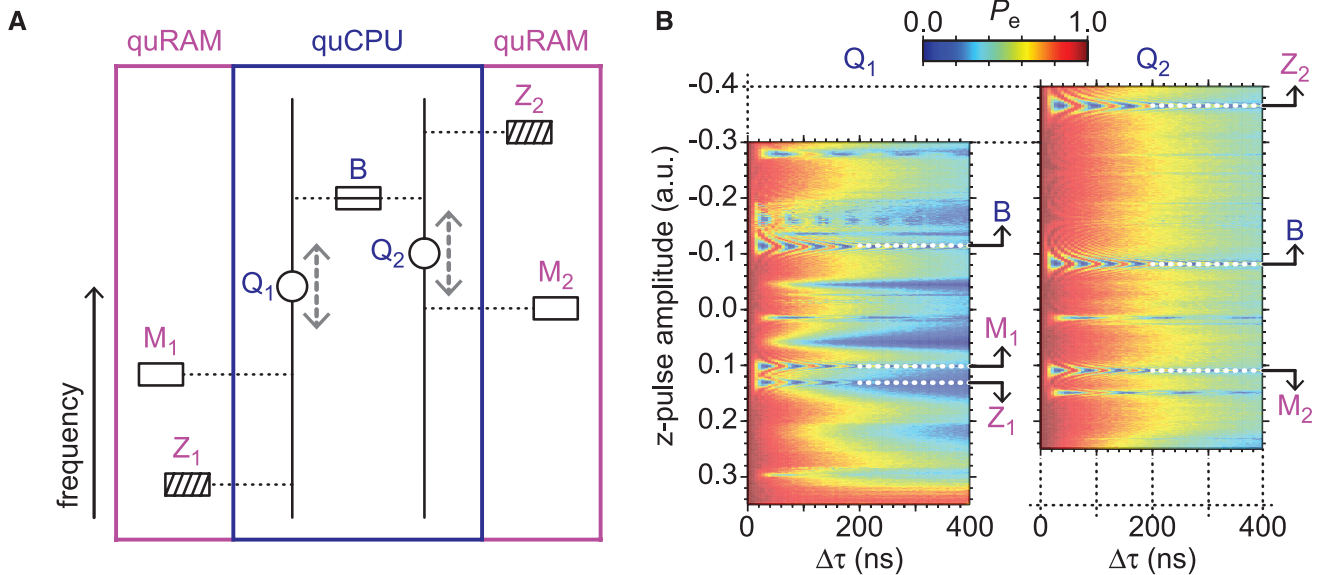


Fig. 1. The quantum von Neumann architecture. **(A)** The quCPU (blue box) includes two qubits Q_1 and Q_2 and the bus resonator B. The quRAM (magenta boxes) comprises two memories M_1 and M_2 and two zeroing registers Z_1 and Z_2 . The horizontal dotted lines indicate connections between computational elements. The vertical direction represents frequency, where the memory and zeroing registers are fixed in frequency, whereas the qubit transition frequencies can be tuned by z-pulses (gray dashed double arrows). **(B)** Swap spectroscopy (21) for Q_1 (left) and Q_2 (right): Qubit excited state $|e\rangle$ probability P_e (color scale) versus z-pulse amplitude (vertical axis) and delay time $\Delta\tau$ (horizontal axis), after exciting the qubit with a π -pulse. At zero z-pulse amplitude the qubits are at their idle points, where they have an energy relaxation time $T_{\text{rel}} \approx 400$ ns. A separate Ramsey experiment yields the qubits' dephasing time $T_{\text{deph}} \approx 200$ ns. By tuning the z-pulse amplitude, the qubit

transition frequencies f_{Q_1} and f_{Q_2} can be varied between ≈ 5.5 and 8 GHz. For z-pulse amplitudes indicated by B and M_1 for Q_1 , and by B and M_2 for Q_2 , the chevron pattern of a qubit-resonator interaction is observed (21). The transition frequencies of B, M_1 , and M_2 are $f_B = 6.82$ GHz, $f_{M_1} = 6.29$ GHz, and $f_{M_2} = 6.34$ GHz, respectively. From the chevron oscillation, we obtain the qubit-resonator coupling strengths, which for both the resonator bus and the memories are ≈ 20 MHz (splitting) for the $|g\rangle \leftrightarrow |e\rangle$ qubit transition, and $\approx \sqrt{2}$ faster for the $|e\rangle \leftrightarrow |f\rangle$ transition ($|g\rangle, |e\rangle$, and $|f\rangle$ are the three lowest qubit states) (22). For all resonators, $T_{\text{rel}} \approx 4$ μs . Swap spectroscopy also reveals that the qubits interact with several modes associated with spurious two-level systems. Two of them, Z_1 and Z_2 , are used as zeroing registers. Their transition frequencies are $f_{Z_1} = 6.08$ GHz and $f_{Z_2} = 7.51$ GHz, respectively, with coupling strength to the qubits of ≈ 17 MHz.

using 70 values of ϕ . Figure 3E shows three examples of $\hat{\rho}_\phi$ for $\phi = 0.28$, $\phi = \pi/2$, and $\phi = \pi$, respectively.

The state generated using $\phi = \pi/2$ plays a central role in the implementation of the two-qubit quantum Fourier transform. Neglecting bit-order reversal, the quantum Fourier transform can be realized by applying a Hadamard gate to Q_2 , followed by a $CZ-\pi/2$ gate between Q_1 and Q_2 , and finally a Hadamard on Q_1 (2, 7, 9), as sketched in Fig. 3F (top left). Representing the input state of the transform as $|x\rangle$ (position) and the output as $|p\rangle$ (momentum), assuming $|x\rangle \in M_2$ and the indexes x and p are integers, with $p \in \{0, 1, 2, 3\}$, the output state is $|p\rangle = \sum_{x=0}^3 e^{i2\pi xp/4} |x\rangle/2$, corresponding to a 4×4 unitary operator. This operator can be fully characterized by means of quantum process tomography (2, 18), which allows us to obtain the χ_m^p matrix (2, 18) shown in Fig. 3F (bottom).

Finally, by combining the $CZ-\phi$ and zeroing gates, we can implement a Toffoli-class gate (10, 12, 27), the three-qubit OR phase gate. This gate, combined with single-qubit rotations, is sufficient for universal computation. A Toffoli gate is a doubly controlled quantum operation, where a unitary operation is applied to a target qubit subject to the state of two control qubits. The canonical Toffoli is a doubly controlled NOT gate; here, we consider a doubly controlled phase gate, which is equivalent through a change of basis of the target qubit. In the canonical Toffoli gate, the control gate is applied if both control qubits, Q_1 AND Q_2 , are in state $|e\rangle$. In our case, the control gate is applied conditionally if the controls Q_1 OR Q_2 are in $|e\rangle$. Additionally, we have implemented a three-qubit gate for the logical function exclusive OR (XOR), which, even though not a Toffoli-class gate, helps to understand the more complex OR gate.

The quantum logic circuits for the XOR and OR gates are drawn in Fig. 4, A and D. The control qubits are Q_1 and Q_2 , and the target is the bus resonator B, effectively acting as the third qubit (as only the states $|0\rangle$ and $|1\rangle$ of B are used). The XOR gate is realized as a series of two $CZ-\pi$ gates between the controls and the target, and the OR gate as the series $\frac{1}{2} CZ-\pi$, $CZ-\pi$, and $\frac{1}{2} CZ-\pi$, in an M-shaped configuration.

The truth table for the XOR gate is displayed in Fig. 4B (top). The control qubits Q_1 and Q_2 are assumed to be in one of the states in M_2 , whereas the target B is in $|0\rangle + |1\rangle$. The target acquires a phase π , corresponding to a “true” result, only when the controls are in the state $|Q_1 Q_2\rangle = |ge\rangle$ or $|eg\rangle$. For the other non-trivial case $|Q_1 Q_2\rangle = |ee\rangle$, the target acquires 0 phase, corresponding to a “false” result. This is due to the action of the two $CZ-\pi$ gates, giving a global phase π when either of the controls

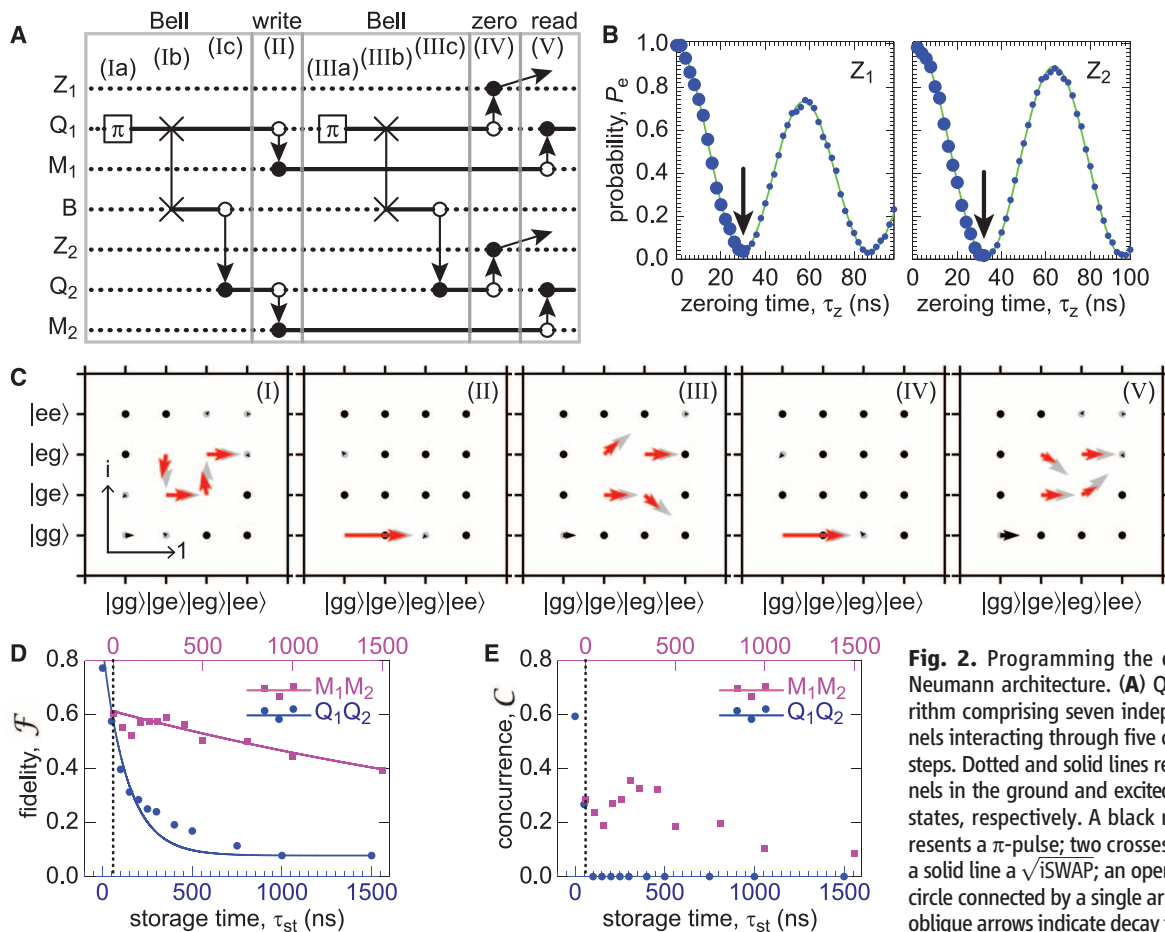


Fig. 2. Programming the quantum von Neumann architecture. **(A)** Quantum algorithm comprising seven independent channels interacting through five computational steps. Dotted and solid lines represent channels in the ground and excited/superposition states, respectively. A black rectangle represents a π -pulse; two crosses connected by a solid line a \sqrt{i} SWAP; an open and a closed circle connected by a single arrow an iSWAP; oblique arrows indicate decay from a zeroing register. **(B)** Calibration of the zeroing gates. The probability P_e measured, with P_e plotted versus τ_z (large and small blue circles). The solid green line is a decaying cosine fit to the data. The black arrows indicate the zeroing time for each qubit. **(C)** Density matrices $\hat{\rho}_{(I)}, \hat{\rho}_{(II)}, \dots, \hat{\rho}_{(V)}$ of the Q_1 - Q_2 state for each step in (A) (scale key on bottom left). Gray arrows, ideal state. Red and black arrows and black dots, measured state (black arrows indicate errors). The off-diagonal elements of $\hat{\rho}_{(I)}, \hat{\rho}_{(II)},$ and $\hat{\rho}_{(V)}$ have different angles because of dynamic phases (26). Fidelities: $\mathcal{F}_{(I)} = 0.772 \pm 0.003$, $\mathcal{F}_{(II)} = 0.916 \pm 0.002$, $\mathcal{F}_{(III)} = 0.689 \pm 0.003$, $\mathcal{F}_{(IV)} = 0.913 \pm 0.002$, and $\mathcal{F}_{(V)} = 0.606 \pm 0.003$. Concurrences: $C_{(I)} = 0.593 \pm 0.006$, $C_{(II)} = 0.029 \pm 0.005$, $C_{(III)} = 0.436 \pm 0.007$, $C_{(IV)} = 0.019 \pm 0.005$, and $C_{(V)} = 0.345 \pm 0.008$. **(D)** Comparison of fidelity \mathcal{F} as a function of storage time τ_{st} for a Bell state stored in Q_1 and Q_2 (blue circles) versus that stored in M_1 and M_2 (magenta squares; error bars smaller than symbols). The solid lines are exponential fits to data. **(E)** As in (D), but for the concurrence C . In (D) and (E), the vertical black dotted line indicates the time delay (≈ 59 ns) associated with memory storage, with respect to storage in the qubits, due to the writing and reading operations (II) and (V) in (A).

Each qubit is prepared in $|e\rangle$, interacts on resonance with its zeroing register for a time τ_z , and its probability P_e measured, with P_e plotted versus τ_z (large and small blue circles). The solid green line is a decaying cosine fit to the data. The black arrows indicate the zeroing time for each qubit. **(C)** Density matrices $\hat{\rho}_{(I)}, \hat{\rho}_{(II)}, \dots, \hat{\rho}_{(V)}$ of the Q_1 - Q_2 state for each step in (A) (scale key on bottom left). Gray arrows, ideal state. Red and black arrows and black dots, measured state (black arrows indicate errors). The off-diagonal elements of $\hat{\rho}_{(I)}, \hat{\rho}_{(II)},$ and $\hat{\rho}_{(V)}$ have different angles because of dynamic phases (26). Fidelities: $\mathcal{F}_{(I)} = 0.772 \pm 0.003$, $\mathcal{F}_{(II)} = 0.916 \pm 0.002$, $\mathcal{F}_{(III)} = 0.689 \pm 0.003$, $\mathcal{F}_{(IV)} = 0.913 \pm 0.002$, and $\mathcal{F}_{(V)} = 0.606 \pm 0.003$. Concurrences: $C_{(I)} = 0.593 \pm 0.006$, $C_{(II)} = 0.029 \pm 0.005$, $C_{(III)} = 0.436 \pm 0.007$, $C_{(IV)} = 0.019 \pm 0.005$, and $C_{(V)} = 0.345 \pm 0.008$. **(D)** Comparison of fidelity \mathcal{F} as a function of storage time τ_{st} for a Bell state stored in Q_1 and Q_2 (blue circles) versus that stored in M_1 and M_2 (magenta squares; error bars smaller than symbols). The solid lines are exponential fits to data. **(E)** As in (D), but for the concurrence C . In (D) and (E), the vertical black dotted line indicates the time delay (≈ 59 ns) associated with memory storage, with respect to storage in the qubits, due to the writing and reading operations (II) and (V) in (A).

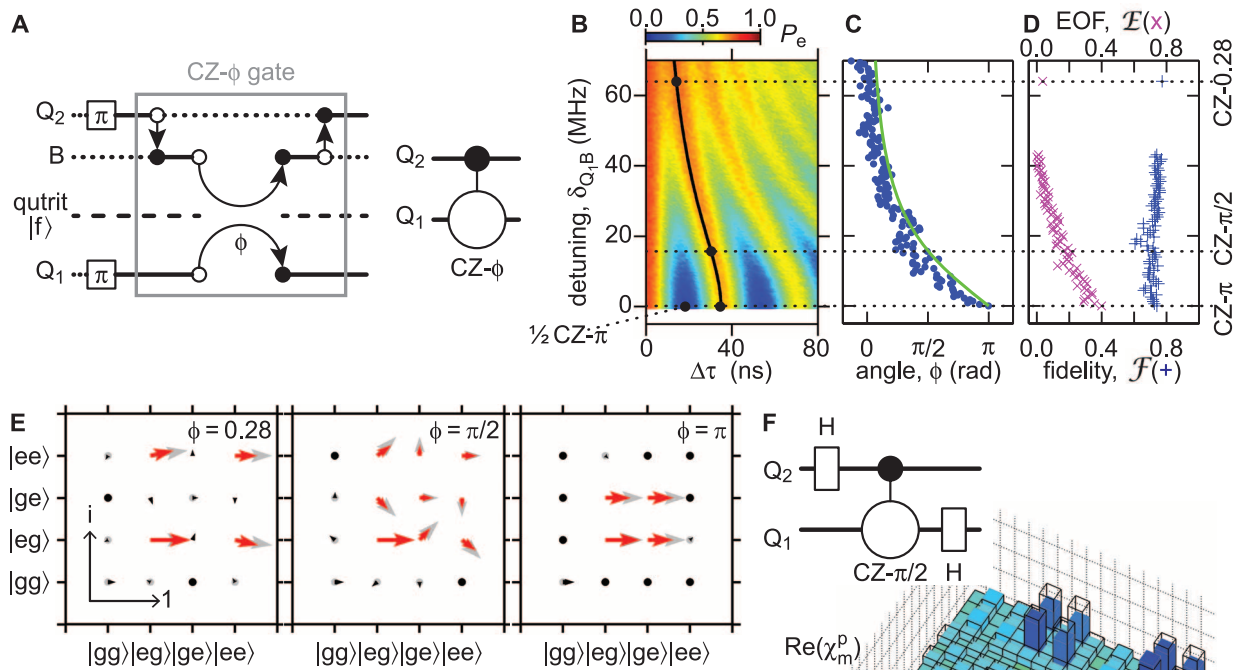


Fig. 3. The quantum Fourier transform. **(A)** (Left) Quantum logic circuit of a CZ- ϕ gate (enclosed in a gray box) for $|Q_1 Q_2\rangle = |ee\rangle$. The $|f\rangle$ state of Q_1 is indicated by a dashed line. The process where Q_1 acquires the phase ϕ is represented by a pair of open/closed circles, connected by a single arrow in an arc shape. All other symbols are as in Fig. 2A. (Right) Shorthand symbol for the CZ- ϕ gate. Although the gate unitary matrix is symmetric, the symbol shows the asymmetric implementation of the gate. **(B)** Time-domain swaps between the states $|Q_1 B\rangle = |e1\rangle$ and $|f0\rangle$, where we plot the probability P_e (color scale) versus interaction time $\Delta\tau$ and detuning δ_{Q1B} . The solid black line indicates combinations of interaction time and detuning that completely depopulate the non-computational $|f\rangle$ state. The three black dots on this line correspond to a CZ- π , CZ- $\pi/2$, and CZ-0.28 gate (see far right). The fourth black dot (outside the line) corresponds to a $1/2$ CZ- π gate (see bottom left), where the $|e\rangle$ state has been shelved to the noncomputational $|f\rangle$ state. **(C)** Phase ϕ acquired by Q_1 as a function of δ_{Q1B} . The blue dots indicate experimental data and the solid green line the theory of Eq. 1 (26). **(D)** Fidelity \mathcal{F} (blue + symbols) and EOF (magenta \times symbols) of measured density matrices $\hat{\rho}_\phi$ versus δ_{Q1B} . **(E)** (Left to right) Density matrices $\hat{\rho}_\phi = \hat{\rho}_{0.28}, \hat{\rho}_{\pi/2}$, and $\hat{\rho}_\pi$, obtained when $\phi = 0.28, \phi = \pi/2$, and $\phi = \pi$ rad in Eq. 2 (scale key on bottom left). The arrows are color coded as in Fig. 2C. The measured fidelities are $\mathcal{F}_{0.28} = 0.751 \pm 0.064$, $\mathcal{F}_{\pi/2} = 0.735 \pm 0.017$, and $\mathcal{F}_\pi = 0.741 \pm 0.030$; and EOFs are $\mathcal{E}_{0.28} = 0.020 \pm 0.055$ (lower bound $\mathcal{E}_{0.28} = 0$), $\mathcal{E}_{\pi/2} = 0.106 \pm 0.031$, and $\mathcal{E}_\pi = 0.401 \pm 0.062$. **(F)** (Top left) Logic circuit for a two-qubit quantum Fourier transform. (Bottom) Real part of the corresponding χ_m^p matrix (2, 18). The process fidelity for the real and imaginary (not shown) part of χ_m^p is $\mathcal{F}_\chi = 0.657 \pm 0.014$. The confidence intervals are estimated from 10 measurements for $\hat{\rho}_{0.28}$, 6 for $\hat{\rho}_{\pi/2}$ and $\hat{\rho}_\pi$, and 15 for χ_m^p .

is in $|e\rangle$ and a phase 2π (equivalent to a 0 phase) when both are in $|e\rangle$.

The truth table can be experimentally measured by performing Ramsey experiments on the target, one for each pair of control states. The experiments are realized by (i) preparing Q_2 in the superposition state $|g\rangle + |e\rangle$ by means of a $\pi/2$ -pulse; (ii) moving the state from Q_2 into B, thus creating a $|0\rangle + |1\rangle$ state in B; (iii) preparing Q_1 and Q_2 in each possible pair of control states in M_2 by means of π -pulses; (iv) performing the XOR gate; (v) zeroing Q_2 into Z_2 at the end of the XOR gate; (vi) moving the final target state from B into the zeroed Q_2 ; and (vii) completing the Ramsey sequence on Q_2 with a second $\pi/2$ -pulse with variable rotation axis relative to the pulse in (i). The measurement outcomes are displayed in Fig. 4B (bottom), together with the least-squares fits used to extract the phase information associated with each value of the

truth table. The Ramsey fringes for the two control states $|ge\rangle$ and $|eg\rangle$ are inverted relative to the reference state $|gg\rangle$, as expected from the XOR gate truth table.

In general, given the Q_1 - Q_2 -B basis set $M_3 = \{|gg0\rangle, |gg1\rangle, |ge0\rangle, |ge1\rangle, |eg0\rangle, |eg1\rangle, |ee0\rangle, |ee1\rangle\}$, the vector τ_k^{XOR} of the diagonal elements associated with the ideal unitary matrix of the XOR gate reads

$$\tau_k^{\text{XOR}} = (1, 1, 1, -1, 1, -1, 1, 1) \quad (3)$$

whereas all off-diagonal elements of the matrix are zero. Each element τ_k^{XOR} can be expressed as a complex exponential $e^{i\phi_{|lmn\rangle}}$, with $|lmn\rangle \in M_3$. The phase $\phi_{|lmn\rangle}$ can be either 0, when $\tau_k^{\text{XOR}} = 1$, or π , when $\tau_k^{\text{XOR}} = -1$. Among the eight values of $\phi_{|lmn\rangle}$, only seven are physically independent, as the element $e^{i\phi_{|gg0\rangle}}$ can be factored, reducing

the set of possible phases to $\phi_{|lmn\rangle} - \phi_{|gg0\rangle}$, with $|lmn\rangle \in M_3 - \{|gg0\rangle\}$.

In analogy to the truth table for the target B, a table with four phase differences can also be obtained for the controls Q_1 and Q_2 , resulting in a total of 12 phase differences. These differences can be measured by performing Ramsey experiments both on the target and the control qubits. It can be shown that from the 12 phase differences, one can obtain the seven independent phases associated with the diagonal elements τ_k^{XOR} (26), thus realizing a quantum phase tomography of the Toffoli gate (28). Figure 4C displays the phase tomography results for our experimental implementation of the XOR gate.

The truth table associated with the M gate is reported in Fig. 4E (top), where the only difference from the XOR gate is the phase π acquired by the target B when the controls Q_1 and

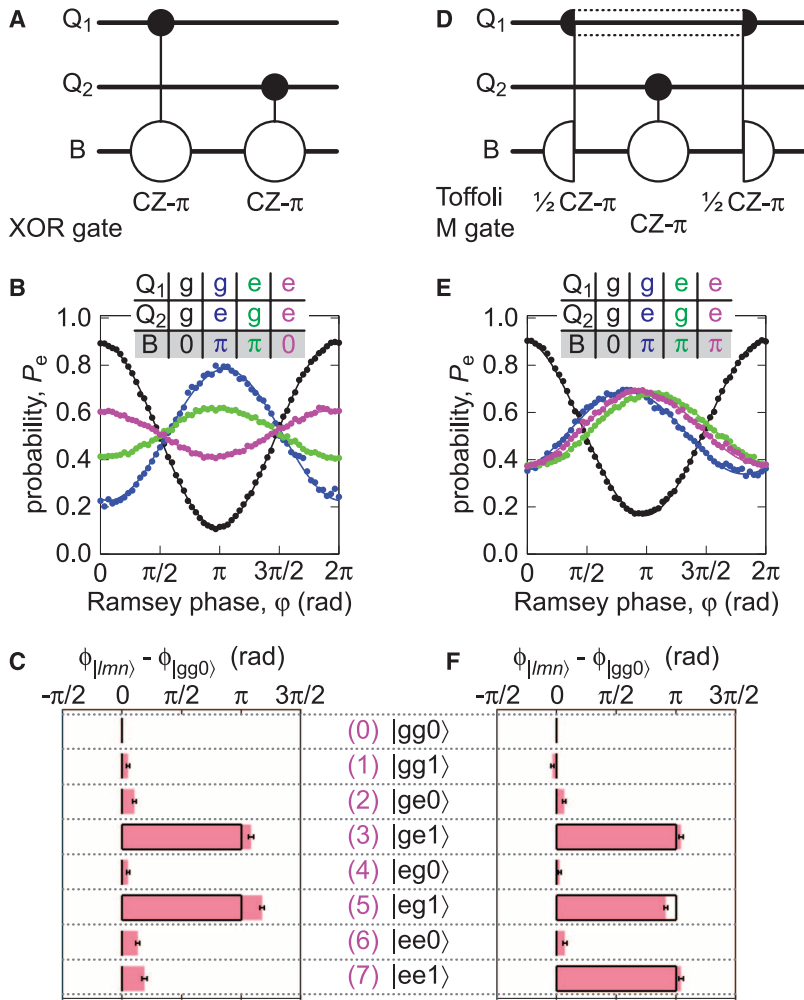


Fig. 4. Three-qubit gates: The XOR phase gate and the Toffoli-class M gate. **(A)** Quantum logic circuit for the XOR phase gate. **(B)** (Top) XOR gate truth table. (Bottom) Ramsey fringes associated with the truth table, showing the probability P_e of measuring Q_2 in $|e\rangle$, versus the Ramsey phase ϕ , for the control input states in M_2 . Black and magenta dots, 0 phase. Blue and green dots, π phase. The solid lines are least-squares fits to the data used to extract the truth-table phases. **(C)** Quantum phase tomography for the XOR gate. Phase $\phi_{|lmn\rangle} - \phi_{|gg0\rangle}$ for each state $|lmn\rangle \in M_3$. Black open boxes, ideal values. Pink areas, measured values with corresponding confidence intervals (black lines). **(D)** Quantum logic circuit for the M gate, implemented as a $\frac{1}{2}$ CZ- π gate (see Fig. 3B) between Q_1 and B (half-dot/half-open circle connected by solid line), followed by a CZ- π gate between Q_2 and B, and a second $\frac{1}{2}$ CZ- π gate between Q_1 and B. The dotted black lines connecting the two $\frac{1}{2}$ CZ- π gates indicate qubit shelving to the $|f\rangle$ state. **(E)** As in (B), but for the M gate. **(F)** As in (C), but for the M gate.

Q_2 are loaded in state $|Q_1 Q_2\rangle = |ee\rangle$. In this case, the action of the first $\frac{1}{2}$ CZ- π gate between Q_1 and B shelves the $|1\rangle$ state from B to the non-computational state $|f\rangle$ in Q_1 , where it remains until the second $\frac{1}{2}$ CZ- π gate. Moving the state of Q_1 outside the computational space during the intermediate CZ- π gate between Q_2 and B effectively turns off the CZ- π gate (12, 29). The target B thus only acquires a total phase π due to the combined action of the two $\frac{1}{2}$ CZ- π gates (see Figure 4D). The experimental truth table obtained from Ramsey fringes is shown in Fig. 4E (bottom).

The vector τ^M of the diagonal elements associated with the ideal unitary matrix of the M gate is $\tau^M = (1, 1, 1, -1, 1, -1, 1, -1)$. A similar

procedure as for the XOR gate allows us to obtain the quantum phase tomography of the M gate (Fig. 4F).

Quantum phase tomography makes it possible to define the phase fidelity of the XOR and M gate,

$$\mathcal{F}_\phi \equiv 1 - \frac{\epsilon_\phi}{\pi} \quad (4)$$

where ϵ_ϕ is the gate root-mean-square phase error, with an upper bound of π . For the XOR gate we find that $\mathcal{F}_\phi = 0.954 \pm 0.004$, and for the M gate $\mathcal{F}_\phi = 0.979 \pm 0.003$.

Our results provide optimism for the near-term implementation of a larger-scale quantum

processor (1–3) based on superconducting circuits. Our architecture shows that proof-of-concept factorization algorithms (2, 3, 5) and simple quantum error correction codes (2, 3, 6, 8) might be achievable using this approach.

References and Notes

1. D. P. DiVincenzo, *Fortschr. Phys.* **48**, 771 (2000).
2. M. A. Nielsen, I. L. Chuang, *Quantum Computation and Quantum Information* (Cambridge Univ. Press, Cambridge, 2000).
3. N. D. Mermin, *Quantum Computer Science: An Introduction* (Cambridge Univ. Press, Cambridge, 2007).
4. H. M. Wiseman, G. J. Milburn, *Quantum Measurement and Control* (Cambridge Univ. Press, Cambridge, 2010).
5. L. M. K. Vandersypen *et al.*, *Nature* **414**, 883 (2001).
6. D. G. Cory *et al.*, *Phys. Rev. Lett.* **81**, 2152 (1998).
7. Y. S. Weinstein, M. A. Pravia, E. M. Fortunato, S. Lloyd, D. G. Cory, *Phys. Rev. Lett.* **86**, 1889 (2001).
8. R. Blatt, D. Wineland, *Nature* **453**, 1008 (2008).
9. J. Chiaverini *et al.*, *Science* **308**, 997 (2005).
10. T. Monz *et al.*, *Phys. Rev. Lett.* **102**, 040501 (2009).
11. D. J. Reilly *et al.*, *Science* **321**, 817 (2008).
12. B. P. Lanyon *et al.*, *Nat. Phys.* **5**, 134 (2009).
13. K. S. Choi, H. Deng, J. Laurat, H. J. Kimble, *Nature* **452**, 67 (2008).
14. J. Clarke, F. K. Wilhelm, *Nature* **453**, 1031 (2008).
15. J. H. Plantenberg, P. C. de Groot, C. J. P. M. Harmans, J. E. Mooij, *Nature* **447**, 836 (2007).
16. L. DiCarlo *et al.*, *Nature* **460**, 240 (2009).
17. P. J. Leek *et al.*, *Phys. Rev. B* **79**, 180511R (2009).
18. T. Yamamoto *et al.*, *Phys. Rev. B* **82**, 184515 (2010).
19. M. Neeley *et al.*, *Nature* **467**, 570 (2010).
20. L. DiCarlo *et al.*, *Nature* **467**, 574 (2010).
21. M. Mariantoni *et al.*, *Nat. Phys.* **7**, 287 (2011).
22. H. Wang *et al.*, *Phys. Rev. Lett.* **106**, 060401 (2011).
23. M. D. Reed *et al.*, *Appl. Phys. Lett.* **96**, 203110 (2010).
24. R. Horodecki, P. Horodecki, M. Horodecki, K. Horodecki, *Rev. Mod. Phys.* **81**, 865 (2009).
25. F. W. Strauch *et al.*, *Phys. Rev. Lett.* **91**, 167005 (2003).
26. Materials and methods are available as supporting material on Science Online.
27. A. Barenco *et al.*, *Phys. Rev. A* **52**, 3457 (1995).
28. A full gate characterization by quantum process tomography was not possible because we could only simultaneously measure two qubits, with the resonator acting as the third qubit.
29. T. C. Ralph, K. J. Resch, A. Gilchrist, *Phys. Rev. A* **75**, 022313 (2007).

Acknowledgments: This work was supported by Intelligence Advanced Research Projects Activity (IARPA) under ARO award W911NF-08-1-0336 and under Army Research Office (ARO) award W911NF-09-1-0375. M.M. acknowledges support from an Elings Postdoctoral Fellowship. Devices were made at the University of California Santa Barbara Nanofabrication Facility, a part of the NSF-funded National Nanotechnology Infrastructure Network. The authors thank A. G. Fowler for useful comments on scalability, and M. H. Devoret and R. J. Schoelkopf for discussions on Toffoli gates. M.M. performed the experiments and analyzed the data. M.M. and H.W. fabricated the sample. T.Y., H.W., and Y.Y. helped with the Fourier transform, and M.N. with three-qubit gates. M.M., A.N.C., and J.M.M. conceived the experiment and cowrote the manuscript.

Supporting Online Materials

www.sciencemag.org/cgi/content/full/science.1208517/DC1
Materials and Methods
Figs. S1 to S12
Tables S1 to S3
References

17 May 2011; accepted 19 July 2011
Published online 1 September 2011;
10.1126/science.1208517